



Article

Modeling of Biologically Effective Daily Radiant Exposures over Europe from Space Using SEVIRI Measurements and MERRA-2 Reanalysis

Agnieszka Czerwińska and Janusz Krzyścin *

Institute of Geophysics, Polish Academy of Sciences, 01-452 Warsaw, Poland; aczerwinska@igf.edu.pl

* Correspondence: jkrzys@igf.edu.pl

Abstract: Ultraviolet solar radiation at the Earth's surface significantly impacts both human health and ecosystems. A biologically effective daily radiant exposure (BEDRE) model is proposed for various biological processes with an analytical formula for its action spectrum. The following processes are considered: erythema formation, previtamin D3 synthesis, psoriasis clearance, and inactivation of SARS-CoV-2 virions. The BEDRE model is constructed by multiplying the synthetic BEDRE value under cloudless conditions by a cloud modification factor (CMF) parameterizing the attenuation of radiation via clouds. The CMF is an empirical function of the solar zenith angle (SZA) at midday and the daily clearness index from the Spinning Enhanced Visible and Infrared Imager (SEVIRI) measurements on board the second-generation Meteosat satellites. Total column ozone, from MERRA-2 reanalysis, is used in calculations of clear-sky BEDRE values. The proposed model was trained and validated using data from several European ground-based spectrophotometers and biometers for the periods 2014–2023 and 2004–2013, respectively. The model provides reliable estimates of BEDRE for all biological processes considered. Under snow-free conditions and $SZA < 45^\circ$ at midday, bias and standard deviation of observation-model differences are approximately $\pm 5\%$ and 15% , respectively. The BEDRE model can be used as an initial validation tool for ground-based UV data.

Keywords: UV radiation; satellite observations; reanalysis; biological effects; erythema appearance; previtamin D3 synthesis; psoriasis clearance; inactivation SARS-CoV-2 virions



Citation: Czerwińska, A.; Krzyścin, J. Modeling of Biologically Effective Daily Radiant Exposures over Europe from Space Using SEVIRI Measurements and MERRA-2 Reanalysis. *Remote Sens.* **2024**, *16*, 3797. <https://doi.org/10.3390/rs16203797>

Academic Editor: Dimitris Kaskaoutis

Received: 28 August 2024
Revised: 8 October 2024
Accepted: 10 October 2024
Published: 12 October 2024



Copyright: © 2024 by the authors. Licensee MDPI, Basel, Switzerland. This article is an open access article distributed under the terms and conditions of the Creative Commons Attribution (CC BY) license (<https://creativecommons.org/licenses/by/4.0/>).

1. Introduction

Surface solar ultraviolet (UV) radiation has gained significant attention in recent decades due to its well-documented harmful and beneficial effects on human health. Harmful effects are associated with skin diseases, including fatal melanoma, DNA mutation, cataracts, and skin ageing, while beneficial effects include the synthesis of vitamin D3 in the skin and removal of psoriatic lesions [1–10].

The first instrument, the Robertson–Berger (RB) biometer, with spectral sensitivity resembling typical human skin sensitivity with respect to erythema appearance, was constructed by the Skin and Cancer Clinic of Temple University, Philadelphia, PA, USA, in the early 1970s [11]. Continuous monitoring of the erythemally effective irradiance began in Europe at Belsk, Poland, in May 1975 [12]. The next long-term UV series started at Norrköping in 1983 [13]. The RB biometer had no temperature stabilization; thus, new improved types of broad-band instruments appeared in the 1990s, which were designed by Solar Light (Philadelphia), Yankee Environmental Systems (Turners Falls, MA, USA), and Kipp and Zonen Co. (Delft, The Netherlands). There were substantial differences between irradiances measured with biometers of the same type, which led to the development of the standardized calibration procedure [14]. Difficulties in maintaining high-quality UV measurements have slowed the use of biometers at standard weather stations. Currently, there are national UV measurement networks in European countries that consist of a limited

number of biometers and much rarer spectral instruments (e.g., the Brewer and Bentham radiometer) [15].

The need to have UV data over a wider area has prompted the development of satellite-based UV data acquisition from the Earth's surface. Today, we have unlimited access to the results of two UV data products using satellite data. Ozone Monitoring Instrument (OMI) surface UV data (OMI_UV) are estimated from a surface UV irradiance algorithm using OMI measurements on board the EOS Aura satellite [16]. OMI operates in the ultraviolet-visible (UV-VIS) spectral range at wavelengths from 270 nm to 500 nm, which are essential for UV-related research. The Finnish Meteorological Institute and NASA Goddard Space Flight Center has maintained the OMI Surface UV Irradiance and Erythemal Dose data product since 2004. The Royal Netherland Meteorological Institute (KNMI) established the Tropospheric Emission Monitoring Service (TEMIS) in 2001, and the TEMIS_UV data started in 2003 (<https://www.temis.nl/uvradiation/product/>, accessed on 26 August 2024).

OMI's surface UV algorithm estimates UV irradiance by correcting for the attenuation effects of ozone, aerosols, surface albedo, and clouds. The OMI_UV retrieval uses measurements of total column ozone (TCO_3) and ground reflectivity at 360 nm wavelength (to parameterize UV attenuation via clouds) obtained during one or two satellite overpasses per day [16]. The TEMIS_UV retrieval takes into account cloud cover data obtained via the Spinning Enhanced Visible and Infrared Imager (SEVIRI) instrument operating on board the Meteosat Second Generation (MSG) satellites [17]. Both retrievals estimate daily values of erythemal radiant exposures (EREs) as the daily integral of erythemal irradiance multiplying synthetic clear-sky erythemal irradiance radiance (OMI_UV and TEMIS_UV using [18,19] models, respectively) with the so-called cloud modification factor (CMF_{ERYT}) parameterizing attenuation of the erythemal irradiance due to clouds. Erythemal irradiance is responsible for erythema (sunburn) formation with maximum sensitivity in the UV-B region (about 297 nm). TEMIS_UV also provides biologically effective daily radiant exposures (BEDREs) for two additional biological effects: previtamin D3 synthesis and DNA damage. As with erythema formation, dermal synthesis of previtamin D3 and the process of DNA destruction are the most effective in the UVB wavelength range (290–315 nm).

In this study, we present a model to calculate BEDRE for any biological process with sensitivity to solar irradiance described by the corresponding action spectrum (AS). The results are obtained for the following biological effects: erythema formation, previtamin D3 synthesis, psoriasis clearance, and inactivation of SARS-CoV-2 virions (causing COVID-19 disease, which continues to be a global health problem (<https://www.who.int/emergencies/diseases/novel-coronavirus-2019/situation-reports/>, accessed on 26 August 2024)). The proposed model can be easily extended to any biological process by using the so-called conversion factors from erythema to other biologically weighted irradiance according to the algorithm proposed by Czerwińska and Krzyścin (2024) [20]. We refer to this model as the Universal Biological Effective (UBE) model, as it can directly compute BEDRE values for any biological effect with a known sensitivity to UV radiation.

The structure of this study is organized as follows. Section 2 outlines the materials and methods used, including a description of the European stations that provide UV data and the model developed to calculate daily radiant exposure (RE) for the selected biological processes. Section 3 presents the results for each biological process, with particular emphasis on validating the proposed model via comparisons with the BEDRE values from several ground-based UV observing stations in Europe using broadband meters and spectrophotometers. Section 4 contains a discussion. Conclusions are presented in Section 5.

2. Materials and Methods

2.1. Ground-Based Measurements of UV Radiation

Table 1 and Figure 1 show the ground-based UV measurement stations included in this study. The UV datasets from all stations, except Belsk, are available from the World Ozone and Ultraviolet Radiation Data Centre (WOUDC, <https://woudc.org>, accessed on

28 August 2024). Data from Belsk are available upon request. The UV measurement results should be calibrated by local authorities before being submitted to the WOUDC database, but this is not always the case. UV measurements from Belsk, Reading, Uccle, and Vienna were used to develop the UBE model, while data from other stations provided a basis for the validation of the proposed model (Section 2.4). Among the stations, Davos is notable as a mountain station where UV radiation is affected by specific clouds and large seasonal variations in albedo.

Table 1. Details of the UV measuring stations used: location, altitude, instrument type, period of the examined, and data source (number of a station in WOUDC database).

Station	Location	Altitude [m a.s.l.]	Instrument	Data Period	Data Source
Belsk Poland	51.85°N, 20.79°E	180	SL Biometer, 501A Kipp&Zonen UV-S-E-T Brewer MK II	2004–2012 2013–2023 2011–2023	Upon request
Reading UK	51.44°N, 0.94°W	66	Bentham DM150	2004–2023	WOUDC No. 353
Uccle Belgium	50.80°N, 4.36°E	100	Brewer MK III	2004–2023	WOUDC No. 053
Diekirch Luxembourg	49.87°N, 6.17°E	218	SL Biometer, 501A	2004–2023	WOUDC No. 412
Vienna Austria	48.26°N, 16.43°E	160	SL Biometer, 501A	2004–2022	WOUDC No. 167
Chisinau Moldavia	47.00°N, 28.82°E	205	Kipp&Zonen UV-S-B-C	2004–2023	WOUDC No. 455
Davos Switzerland	46.82°N, 9.85°E	1590	Kipp&Zonen UV-S-E-T	2007–2023	WOUDC No. 501

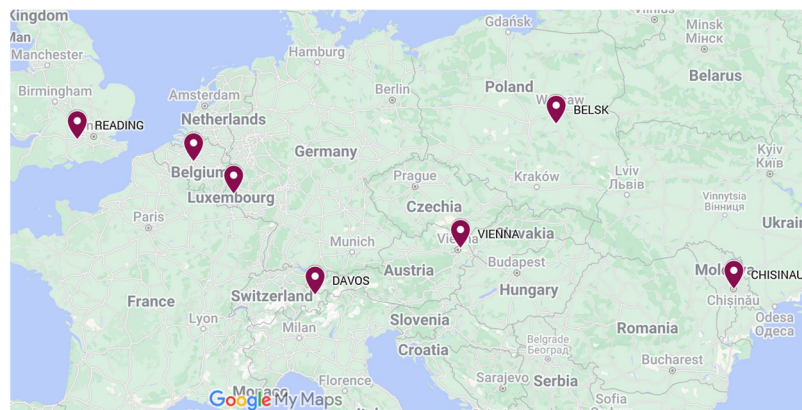


Figure 1. The location of the UV measuring stations shown in Table 1 (created with Google My Maps: Map data 2024).

Recently, Belsk's time series of daily erythemal radiant exposure (ERE) data, which began in 1976, was homogenized. The homogenization procedure for the period 2004–2013 consisted of a comparison of the measured daily ERE during sunny days with the corresponding synthetic daily ERE for cloudless days using the tropospheric ultraviolet and visible radiation (TUV) radiative transfer model [21]. The calibration constants for Belsk's Kipp & Zonen UV-S-E-T biometer (Kipp & Zonen D.V. Delf, The Netherlands) were derived from comparisons of the daily ERE with the collocated well-maintained Brewer Mark II No. 64 spectrophotometer (with a single monochromator, Kipp & Zonen D.V. Delf, The Netherlands) during cloudless days.

In Reading, spectral irradiance has been measured since 2004 using a Bentham DM150 (Bentham Instruments Ltd., Reading, UK) with a double monochromator in the range 290–500 nm, with a spectral resolution of 0.5 nm, every 30 min. The instrument is regularly calibrated with 200 W irradiance standard lamps, which are annually compared with U.S. National Institute of Standards and Technology (NIST) traceable 1000 W lamps. Moreover, the quality of each spectrum was checked with the SHICRivm algorithm [22].

The erythemal irradiances measured with the SL Biometer 501A (Solar Light Company, LLC, Glenside, PA, USA) in Vienna also underwent a strict calibration procedure as this has been applied for each biometer included in the Austrian UV network [15].

For stations equipped with spectral radiometers (e.g., Reading and Uccle), daily ERE values were calculated using CIE 2019 action spectra for erythema [23] applied to the original unweighted spectral irradiances. The time resolution of the spectra was fixed to 30 min for Reading and varied for Uccle (Brewer Mark III, Kipp & Zonen D.V. Delf, The Netherlands). For stations equipped with broad-band Kipp & Zonen biometers (e.g., Belsk, Chisinau, and Davos), erythemally weighted irradiances recorded with 1 min resolution were available, while for the SL biometers (Solar Light Company, LLC, Glenside, PA, USA), the resolution was 30 min in Diekirch and Vienna. The trapezoid formula was applied to estimate the daily (sunrise–sunset) integral of the biologically effective irradiance.

2.2. Ancillary Data

The ancillary data required for this study include TCO_3 , clearness index (CI), and UV satellite data for model validation.

TCO_3 values needed for the clear-sky erythemal irradiance calculations (Section 2.3) were obtained as an average of the hourly TCO_3 data from The Modern-Era Retrospective analysis for Research and Applications, Version 2 (MERRA-2) data [24]. The high quality of MERRA-2 TCO_3 has been supported by numerous comparisons with satellite and ground-based observations [25–27]. The MERRA-2 TCO_3 was available for all days in the 2004–2023 period. From October 2004, the MERRA-2 has used TCO_3 data from the OMI measurements during the data assimilation procedure [25].

The CI is a commonly used parameter describing cloud attenuation of global (direct and diffusive) solar irradiance at ground level [28]. Here, this is expressed as a quotient of the all-sky (G) and corresponding synthetic clear-sky (G_0) daily integral of global solar irradiances. The CI, equal to G/G_0 , is used in estimations of cloud effects on biologically effective radiation (Section 2.3). G and G_0 daily values were taken from MSG data archived by the Copernicus Atmosphere Monitoring Service (CAMS) [29].

The performance of the proposed model will be assessed via comparisons with UV measurements at the stations shown in Table 1. Similar comparisons have also been made using the two existing satellite databases OMI_UV and TEMIS_UV. This will result in a ranking of the models to be established. The Giovanni tool [30] enables obtaining the daily ERE for any site from 1 October 2004 using the Aura-OMI Spectral Surface UVB Irradiance and Erythemal Dose product [31]. The TEMIS_UV dataset used here was TEMIS overpass data files [32,33].

2.3. Model Description

2.3.1. Biologically Weighted Radiant Exposures

The daily value of the biologically weighted radiant exposure for a biological process BIOL in Julian day D , $\text{RE}_{\text{BIOL}}(D)$, is defined as

$$\text{RE}_{\text{BIOL}}(D) = \int_{\text{Sunrise}(D)}^{\text{Sunset}(D)} \text{Ir}_{\text{BIOL}}(t) dt \quad (1)$$

where biologically weighted irradiance, $\text{Ir}_{\text{BIOL}}(t)$, is the integral over the UV wavelengths (UV-B, 290–315 nm, and UV-A range, 315–400 nm) of the spectral irradiance, $\text{Ir}(\lambda, t)$, weighted by the action spectrum $\text{AS}_{\text{BIOL}}(\lambda)$:

$$I_{\text{BIOL}}(t) = \int_{290 \text{ nm}}^{400 \text{ nm}} I_{\text{r}}(\lambda, t) A_{\text{SBIOL}}(\lambda) d\lambda \quad (2)$$

Under clear-sky conditions, $I_{\text{BIOL}}(t)$ and $RE_{\text{BIOL}}(D)$ are denoted as $I_{\text{BIOL,clear-sky}}$ and $RE_{\text{BIOL,clear-sky}}(D)$, respectively.

In this study, the following action spectra are considered: erythema (CIE 2019 [23]), photosynthesis of previtamin D₃ in human skin (CIE 2006 [34]), psoriasis clearing (Krzyściński et al. 2012 [35]), and inactivation of the SARS-CoV-2 viruses (Biasin et al., 2022 [9]). These action spectra are shown in Figure 2. Accordingly, the abbreviations ERYT, VITD, PSOR, and SARS are used to calculate $RE_{\text{BIOL}}(D)$ for these action spectra.

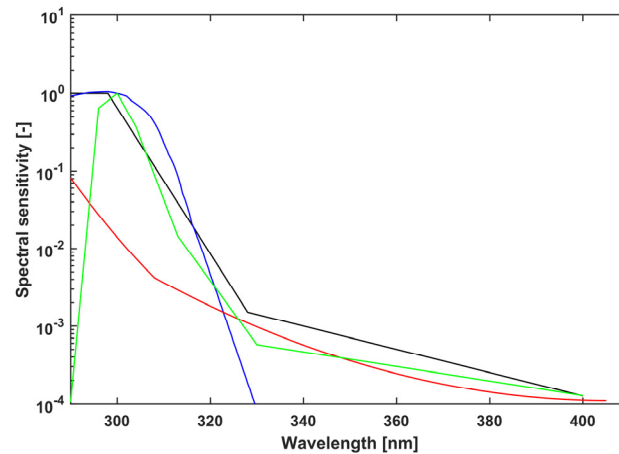


Figure 2. Normalized action spectra for the specific biological effects: erythema appearance (black), photosynthesis of previtamin D₃ in human skin (blue), psoriasis clearance (green), and inactivation of SARS-CoV-2 virions (red).

If the UV spectra are available from measurements, $RE_{\text{BIOL}}(D)$ can be directly calculated using Equation (1). Nowadays biometers provide approximate values of the erythemal irradiance, $I_{\text{ERYT}}(t)$, as their sensitivity to UV radiation differs only slightly from the CIE 2019 standard. The calibration of the biometers allows us to account for the action spectra discrepancies [14].

Frequently, in modeling of the UV irradiance, an assumption is used that $RE_{\text{BIOL}}(D)$ is a part of the synthetic clear-sky $RE_{\text{BIOL,clear-sky}}(D)$ value obtained from radiative transfer simulations because of light scattering by clouds. A formula for the clouds' attenuation can be empirically derived for each considered biological processes using the so-called Cloud Modification Factor (CMF_{BIOL}), which is parameterized here as a power function of CI with α_{BIOL} and β_{BIOL} coefficients:

$$CMF_{\text{BIOL}}(D) = \alpha_{\text{BIOL}} [CI(D)]^{\beta_{\text{BIOL}}} \quad (3)$$

This assumption leads to the following version of the model (1):

$$RE_{\text{BIOL}}(D) = \alpha_{\text{BIOL}} [CI(D)]^{\beta_{\text{BIOL}}} RE_{\text{BIOL,clear-sky}}(D) \quad (4)$$

Coefficients α_{BIOL} and β_{BIOL} of the power function are separately estimated for the three stations (Reading, Belsk, and Vienna) using a standard least-squares linear regression model after applying the logarithm to both sides of Equation (4). $RE_{\text{BIOL}}(D)$ is calculated directly from the measured spectral irradiances via radiometers weighted by the erythema action spectrum or from the output of the biometers. The corresponding synthetic clear-sky value ($RE_{\text{BIOL,clear-sky}}$) is estimated using an empirical model of the erythemal irradiance developed by Allaart et al. [19], which has been modified here for other (non-erythemal) biological effects.

The regression coefficients α_{BIOL} and β_{BIOL} were determined using a part of the data, i.e., for the period 2014–2023, and separately for three ranges of the noon SZA (SZA_N), $\text{SZA}_N < 45^\circ$, $\text{SZA}_N \geq 45^\circ$ and $\text{SZA}_N \leq 60^\circ$, and $\text{SZA}_N > 60^\circ$. Table A1 shows the dates on which SZA_N first and last reached the thresholds of 45° and 60° for the considered stations listed in Table 1. The final model uses the power function constants, $\hat{\alpha}_{\text{BIOL}}$ and $\hat{\beta}_{\text{BIOL}}$, averaged over the constants obtained for the three abovementioned stations:

$$\text{RE}_{\text{BIOL}}(D) = \hat{\alpha}_{\text{BIOL}}[\text{CI}(D)]^{\hat{\beta}_{\text{BIOL}}} \text{RE}_{\text{BIOL,clear-sky}}(D) \quad (5)$$

2.3.2. Clear-Sky Radiation

The original model by Allaart et al. [19] estimated the clear-sky erythemal irradiance, $\text{Ir}_{\text{ERYT,clear-sky}}(t)$, as an empirical function of two readily available variables, solar zenith angle (SZA) and TCO_3 . Further in the text, this is denoted as $\text{Ir}_{\text{ERYT_AL}}(\text{SZA}, \text{TCO}_3)$. Standard astronomical formulas of the sun position parameters are used to calculate SZA and the daily mean TCO_3 were taken from MERRA-2 data (Section 2.2). This model was fitted to data collected in De Bilt, The Netherlands, with an elevation of 3 m, typical lowland horizontal visibility (HV) of ~23 km, and albedo (snowless throughout the entire year). Therefore, the original model was modified to account for the erythemal irradiance increase with the elevation of the site (C_{ES}), horizontal visibility (C_{HV}), and surface albedo (C_{SA}). The final formula providing erythemal irradiance, $\text{Ir}_{\text{clear-sky}}^*(t)$, at any site is as follows:

$$\text{Ir}_{\text{clear-sky}}^* = C_{\text{ES}} C_{\text{HV}} C_{\text{SA}} \text{Ir}_{\text{ERYT_AL}}(\text{SZA}, \text{TCO}_3) \quad (6)$$

Simplified formulas are used for C_{ES} (Equation (7)) assuming an increase of 8% with 1 km of altitude [36] and C_{HV} based on the proposed regression formula (Equation (8)) of the erythemal irradiance change with HV (for HV in the range 5–100 km).

$$C_{\text{ES}} = 1 + 0.08H, \quad H \text{ in km} \quad (7)$$

$$C_{\text{HV}} = -1.381 \cdot \text{HV}^{-0.7786} + 1.12, \quad \text{HV in km} \quad (8)$$

C_{HV} was derived from a regression model of clear-sky erythemal irradiance using the fast radiation transfer (FastRT) model [37] with various HV (in km) from 5 km to 100 km. For De Bilt, $H = 0.0$ km, $\text{HV} = 23$ km (representative for sites outside highly agglomerated urban regions [38,39]), and $C_{\text{SA}} = 1$ for snowless surfaces.

For Davos, $\text{HV} = 53$ km was calculated based on the Koshmieder formula [40] estimating aerosol optical depth (AOD) at ~500 nm with HV, $\text{AOD}_{500 \text{ nm}} = -\ln(0.02) \text{HV}^{-1}$, and the mean aerosol optical depth of 0.074 at 500 nm wavelength from AERONET climatology [41].

To calculate the synthetic value of clear-sky biologically weighted irradiances for any biological effect, we use a concept of the conversion factor from erythemal to other non-erythemal irradiance ($\text{CF}_{\text{ERYT} \rightarrow \text{BIOL}}$), which depends on SZA and TCO_3 [20,42].

$$\text{Ir}_{\text{BIOL,clear-sky}} = \text{CF}_{\text{ERYT} \rightarrow \text{BIOL}}(\text{SZA}, \text{TCO}_3) \text{Ir}_{\text{clear-sky}}^*(t) \quad (9)$$

$\text{CF}_{\text{ERYT} \rightarrow \text{BIOL}}$ values for gridded SZA and TCO_3 pairs were calculated for all biological effects considered here [20]. Bilinear interpolations between these gridded values allowed the calculation of the conversion factor for any SZA and TCO_3 pair. Combining Equations (5)–(9), the BEDRE for day D of the year has the following final form:

$$\text{RE}_{\text{BIOL}}(D) = \hat{\alpha}_{\text{BIOL}}[\text{CI}]^{\hat{\beta}_{\text{BIOL}}} C_{\text{ES}} C_{\text{HV}} C_{\text{SA}} \int_{\text{Sunrise}(D)}^{\text{Sunset}(D)} \text{CF}_{\text{ERYT} \rightarrow \text{BIOL}} \text{Ir}_{\text{ERYT_AL}} dt \quad (10)$$

The trapezoid rule was applied in an estimation of the integral value using 1-h means of $\text{Ir}_{\text{ERYT_AL}}(\text{SZA}, \text{TCO}_3)$ and $\text{CF}_{\text{ERYT} \rightarrow \text{BIOL}}(\text{SZA}, \text{TCO}_3)$. $C_{\text{SA}} = 1$ was assumed, i.e., the same albedo was used for all considered stations (Table 1) as that for De Bilt. This assumption will be discussed further in Section 3 when Davos data are discussed.

2.4. Model Validation

Validation of model (10) was carried out for each station individually using standard statistical measures of goodness of fit between measured and modeled $RE_{ERYT}(D)$ values for the period 2004–2013 (Belsk, Reading, and Vienna), 2004–2023 (Uccle, Diekirch, and Chisinau, i.e., the stations not used in UBE training), and 2007–2023 for Davos (since UV measurements began here later than for the other lowland stations considered). In addition, the comparisons are between the measured $RE_{ERYT}(D)$ against OMI_UV and TEMIS_UV models for the period 2004–2013.

For biological effects other than erythema, UV spectral measurements at Belsk, Reading, and Uccle are used in the calculation of $RE_{BIOL}(D)$ and compared with the corresponding UBE and TEMIS_UV (only for previtamin D_3) model values. Finally, we verify the assumption that the cloud attenuation of non-erythemal irradiance based on Equation (3) can be replaced by the cloud attenuation for the erythemal irradiance, i.e., $\hat{\alpha}_{ERYT}$ and $\hat{\beta}_{ERYT}$ can be inserted in place of $\hat{\alpha}_{BIOL}$ and $\hat{\beta}_{BIOL}$ in Equation (10), regardless of the biological process considered.

In model–observation comparison, relative differences between observed ($x_{i, OBS}$) and modeled values ($x_{i, MOD}$) as a percentage of the modeled value, i.e., $100\% (x_{i, OBS} - x_{i, MOD})/x_{i, MOD}$, were examined using standard statistical metrics: mean relative error (MRE), mean absolute error (MAE), root mean square error (RMSE), and standard deviation (SD). For the definition of these descriptive statistics, see, for example, [20].

3. Results

3.1. Erythema Appearance

Table 2 presents regression coefficients α_{ERYT} and β_{ERYT} calculated for Belsk, Reading, and Vienna based on Equation (3) and the UV measurements for the 2014–2023 period. The mean value of these regression coefficients, $\hat{\alpha}_{ERYT}$ and $\hat{\beta}_{ERYT}$, which are used in Equation (10), are in the last row of Table 2. The quality of the proposed model can be supported by a scatter plot of modeled against measured $RE_{BIOL}(D)$ values. Figure 3 shows scatter plots for Belsk using the data for the period 2004–2013 (not used in UBE training), and Figure A1 for Reading and Vienna. In all of these cases, the modeled values correspond to the measured values over the entire range of $RE_{BIOL}(D)$ variability, as evidenced by the pattern of smoothed values via Locally Weighted Scatterplot Smoothing [LOWESS, 43] near the ideal 1–1 (diagonal square) line of agreement. Furthermore, the correlation coefficients between measured and modeled values are very high at around 0.9.

Table 2. Regression coefficients α_{ERYT} and β_{ERYT} to estimate cloud attenuation of the erythemal irradiance calculated for Belsk, Reading, and Vienna for three ranges of the noon solar zenith angle (SZA_N). The average values of the coefficients, $\hat{\alpha}_{ERYT}$ and $\hat{\beta}_{ERYT}$, are in the last row.

Site	Regression Constants					
	α_{ERYT}	β_{ERYT}	α_{ERYT}	β_{ERYT}	α_{ERYT}	β_{ERYT}
	$SZA_N < 45^\circ$		$SZA_N \geq 45^\circ$ and $< 60^\circ$		$SZA_N \geq 60^\circ$	
Belsk	0.954	0.817	0.928	0.755	0.952	0.649
Reading	1.012	0.822	1.018	0.778	1.031	0.727
Vienna	0.951	0.850	0.917	0.743	0.946	0.799
Average	$\hat{\alpha}_{ERYT}$	$\hat{\beta}_{ERYT}$	$\hat{\alpha}_{ERYT}$	$\hat{\beta}_{ERYT}$	$\hat{\alpha}_{ERYT}$	$\hat{\beta}_{ERYT}$
	0.973	0.830	0.954	0.758	0.977	0.725

Table 3 shows the performance of the proposed UBE model, TEMIS_UV, and OMI_UV based on standard statistical metrics applied to the differences between measured and modeled values of $RE_{ERYT}(D)$ in the period 2004–2013 (UV data not used in the model training) as a percentage of the modeled values.

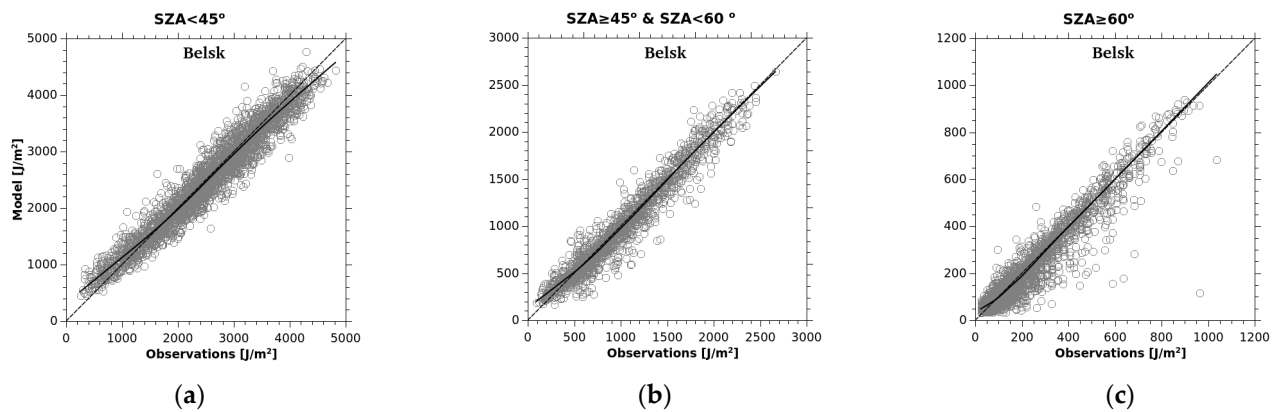


Figure 3. Scatter plot of UBE model against measured daily erythemal radiant exposure at Belsk for all-sky conditions for different ranges of noon SZA: (a) $SZA < 45^\circ$; (b) $SZA \geq 45^\circ$ and $SZA < 60^\circ$; (c) $SZA \geq 60^\circ$. The dotted line is the 1–1 agreement line. The solid curve represents smoothed values from the LOWESS filter [43].

Table 3. Statistical metrics of the differences between the measured and modeled daily erythemal radiant exposures for the 2004–2013 period in percent of the measured values for various noon SZA (SZA_N) ranges for the stations used in the model training.

Metric [%]	Belsk			Reading			Vienna		
	SZA_N <45°	SZA_N [45°, 60°]	SZA_N >60°	SZA_N <45°	SZA_N [45°, 60°]	SZA_N > 60°	SZA_N <45°	SZA_N [45°, 60°]	SZA_N >60°
	UBE model								
MRE	0.49	3.88	4.26	−3.66	−3.39	−0.70	−3.01	1.03	0.11
MAE	9.45	12.97	20.22	9.48	10.66	12.49	9.99	12.19	15.55
RMSE	14.18	18.62	27.35	13.79	15.51	18.72	15.96	17.09	21.20
SD	14.18	18.22	27.03	13.30	15.52	18.71	15.68	17.07	21.22
	TEMIS_UV								
MRE	−13.36	−8.45	−17.33	−20.14	−11.34	−2.63	−15.24	−8.67	−9.16
MAE	14.58	15.23	27.15	20.68	13.70	12.39	16.49	15.59	19.64
RMSE	22.36	25.06	44.10	26.39	19.64	18.66	24.35	23.42	27.15
SD	17.94	23.61	40.57	17.07	16.04	18.48	18.99	21.77	25.57
	OMI_UV								
MRE	1.53	−7.27	−27.01	−18.95	−24.75	−25.39	−1.72	−8.76	−13.37
MAE	13.19	18.50	39.24	21.23	26.31	28.19	12.99	17.86	24.56
RMSE	19.56	27.20	54.72	27.07	32.53	34.60	19.57	25.32	32.75
SD	19.51	26.23	47.56	19.34	21.12	23.51	19.50	23.79	29.92

An improvement in the modeling of daily ERE via the proposed model can be revealed with comparisons of its statistical metric values with those derived via TEMIS_UV and OMI_UV for three subsets of SZA_N . The UBE model has more metric values closer to zero. Using metric values shown for three stations and three SZA_N classes, we found that UBE almost always provides better metrics values when compared with TEMIS_UV. In ~92% of cases (33 out of a total of 36 cases == 3 stations \times 4 metrics \times 3 classes of SZA_N), UBE metric values were closer to zero than those from TEMIS_UV. The remaining three cases were for Reading when $SZA_N \geq 60^\circ$. Comparing UBE with OMI_UV, in ~97% of cases (35 out of a total of 36 cases), UBE performed better. The metric value closest to zero (−1.72%) via OMI_UV was found in Vienna only for MRE when $SZA_N < 45^\circ$.

Table 4 shows the performance of UBE, TEMIS_UV, and OMI_UV models for the stations not used in the UBE training (Diekirch, Uccle, Davos, and Chisinau). Davos is the only mountain station considered here. Chisinau station was excluded from the analysis of the UBE performance because of too large values for MAE and RMSE suggesting problems with the instrument calibration. The comparisons between the statistical metrics of the measurement–model differences support the conclusion of better performance of

Table 5. Performance of all considered models for Davos in the period 2007–2023 in division into highly probable snowless (from 166 day to 227 day of the year) and snow conditions (from 349 to 46 days of the year).

Metric	No-Snow in Davos			Snow in Davos		
	UBE	OMI_UV	Temis_UV	UBE	OMI_UV	Temis_UV
MRE [%]	−0.47	−14.26	−7.27	26.13	25.17	40.60
MAE [%]	11.71	20.25	13.04	27.66	29.80	44.06
RMSE [%]	16.50	30.65	18.78	30.36	33.29	48.76
SD [%]	16.52	27.18	17.35	15.46	21.80	27.02

3.2. Other (Non-Erythemal) Biological Effects

Spectral measurements at three stations (Belsk, Reading, and Uccle) in the period 2014–2023 allow for the calculation of the α_{BIOL} and β_{BIOL} coefficients used in the estimation of cloud attenuation of the biologically weighted irradiance using the SEVIRI global irradiance product (Equations (3) and (4)). For each biological effect considered here, the individual station values of these coefficients and their averaged values, which are used in the final UBE model of $\text{RE}_{\text{BIOL}}(D)$ (Equation (10)), are shown in Table 6. The differences between the averaged values of the coefficients are within a few percent for $\text{SZAN} \leq 60^\circ$. The highest difference between the averaged coefficients of about 13% is found for $\hat{\alpha}_{\text{VITD}}$ (1.107) and $\hat{\alpha}_{\text{SARS}}$ (0.980) for $\text{SZAN} \geq 60^\circ$. Therefore, an additional option of using the cloud coefficients previously obtained for the erythemal effect instead of the non-erythemal coefficients is also considered for the calculation of non-erythemal biological effects.

Table 6. Regression coefficients, α_{BIOL} and β_{BIOL} , to estimate cloud attenuation of the daily biologically effective radiant exposure in the period 2014–2023 for previtamin D₃ synthesis, psoriasis clearance, and inactivation of SARS-Co-2 virions at Belsk, Reading, and Uccle for three ranges of the noon solar zenith angle (SZAN). The average values of these coefficients, $\hat{\alpha}_{\text{BIOL}}$ and $\hat{\beta}_{\text{BIOL}}$, are in the last row of each segment of the Table containing the station coefficients for the selected biological effect. For comparison purposes, the last row of the Table shows the cloud coefficients ($\hat{\alpha}_{\text{ERYT}}$ and $\hat{\beta}_{\text{ERYT}}$) for the erythemal effect according to Table 2.

Site	Regression Constants					
	$\text{SZAN} < 45^\circ$		$\text{SZAN} \geq [45^\circ, 60^\circ]$		$\text{SZAN} > 60^\circ$	
previtamin D ₃ synthesis						
	α_{VITD}	β_{VITD}	α_{VITD}	β_{VITD}	α_{VITD}	β_{VITD}
Belsk	0.968	0.828	0.967	0.714	1.074	0.605
Reading	1.013	0.847	1.039	0.783	1.106	0.732
Uccle	1.063	0.867	1.044	0.776	1.140	0.765
Average	$\hat{\alpha}_{\text{VITD}}$	$\hat{\beta}_{\text{VITD}}$	$\hat{\alpha}_{\text{VITD}}$	$\hat{\beta}_{\text{VITD}}$	$\hat{\alpha}_{\text{VITD}}$	$\hat{\beta}_{\text{VITD}}$
	1.015	0.847	1.017	0.758	1.107	0.700
psoriasis clearance						
	α_{PSOR}	β_{PSOR}	α_{PSOR}	β_{PSOR}	α_{PSOR}	β_{PSOR}
Belsk	0.961	0.829	0.939	0.722	0.950	0.617
Reading	1.014	0.850	1.033	0.792	1.060	0.745
Uccle	1.045	0.867	1.014	0.778	1.058	0.770
Average	$\hat{\alpha}_{\text{PSOR}}$	$\hat{\beta}_{\text{PSOR}}$	$\hat{\alpha}_{\text{PSOR}}$	$\hat{\beta}_{\text{PSOR}}$	$\hat{\alpha}_{\text{PSOR}}$	$\hat{\beta}_{\text{PSOR}}$
	1.007	0.849	0.995	0.764	1.023	0.710
SARS-CoV-2 virions inactivation						
	α_{SARS}	β_{SARS}	α_{SARS}	β_{SARS}	α_{SARS}	β_{SARS}
Belsk	0.935	0.787	0.883	0.710	0.865	0.616
Reading	1.041	0.819	1.043	0.787	1.067	0.756
Uccle	1.003	0.820	0.970	0.757	1.009	0.764
Average	$\hat{\alpha}_{\text{SARS}}$	$\hat{\beta}_{\text{SARS}}$	$\hat{\alpha}_{\text{SARS}}$	$\hat{\beta}_{\text{SARS}}$	$\hat{\alpha}_{\text{SARS}}$	$\hat{\beta}_{\text{SARS}}$
	0.993	0.809	0.965	0.751	0.980	0.711
Erythema Appearance (from Table 2)						
Average	$\hat{\alpha}_{\text{ERYT}}$	$\hat{\beta}_{\text{ERYT}}$	$\hat{\alpha}_{\text{ERYT}}$	$\hat{\beta}_{\text{ERYT}}$	$\hat{\alpha}_{\text{ERYT}}$	$\hat{\beta}_{\text{ERYT}}$
	0.973	0.830	0.954	0.758	0.977	0.725

Table 7 shows the performance of the UBE model for each station and selected biological effects using non-erythemal cloud attenuation coefficients ($\hat{\alpha}_{\text{BIOL}}$ and $\hat{\beta}_{\text{BIOL}}$) and data not included in the model training, i.e., 2004–2013 for Reading and Uccle and 2011–2013 for Belsk. Table 8 shows the corresponding results after applying the erythemal cloud attenuation coefficients ($\hat{\alpha}_{\text{ERYT}}$ and $\hat{\beta}_{\text{ERYT}}$) for all available data, i.e., 2004–2023 for Reading and Uccle and 2011–2023 for Belsk.

Table 7. Performance of the UBE model with the cloud attenuation coefficients for each biological effect ($\hat{\alpha}_{\text{BIOL}}$ and $\hat{\beta}_{\text{BIOL}}$, Table 6) based on the data not used in the model training: 2004–2013 (for Uccle and Reading) and 2011–2013 (for Belsk).

Statistics [%]	Belsk			Uccle			Reading		
	SZA _N <45°	SZA [45°, 60°]	SZA _N >60°	SZA _N <45°	SZA [45°, 60°]	SZA _N >60°	SZA _N <45°	SZA [45°, 60°]	SZA _N >60°
previtamin D ₃ synthesis									
MRE	−10.59	−3.46	1.53	−6.02	−8.04	−8.83	−8.50	−8.94	−9.11
MAE	12.86	14.07	18.32	10.89	12.84	16.64	12.35	13.21	15.60
RMSE	19.24	20.45	24.41	15.64	19.38	24.45	17.90	19.22	22.23
SD	16.09	20.20	24.40	14.44	17.65	22.81	15.75	17.03	20.29
psoriasis clearance									
MRE	−9.75	−1.65	3.80	−6.38	−7.74	−7.08	−7.57	−7.21	−5.66
MAE	12.25	13.30	17.37	10.89	12.07	14.88	11.61	11.82	13.30
RMSE	18.66	19.30	22.93	15.93	18.22	22.61	16.82	17.33	20.13
SD	15.93	19.27	22.64	14.60	16.50	21.48	15.03	15.77	19.34
SARS-CoV-2 virions inactivation									
MRE	−6.51	−0.26	3.96	−6.04	−7.41	−6.40	−2.53	−2.31	−1.31
MAE	9.47	12.19	17.11	9.01	10.82	14.07	8.12	9.03	12.32
RMSE	15.61	18.31	22.55	13.33	16.64	21.45	12.08	13.05	18.61
SD	14.21	18.35	22.23	11.88	14.91	20.48	11.81	12.85	18.56

Table 8. Similar to Table 7 but the UBE model uses $\hat{\alpha}_{\text{ERYT}}$ and $\hat{\beta}_{\text{ERYT}}$ (Table 2) and the statistical metrics are derived from all available spectral data: 2004–2023 (for Uccle and Reading) and 2011–2023 (for Belsk).

Statistics [%]	Belsk			Uccle			Reading		
	SZA _N <45°	SZA [45°, 60°]	SZA _N >60°	SZA _N <45°	SZA [45°, 60°]	SZA _N >60°	SZA _N <45°	SZA [45°, 60°]	SZA _N >60°
previtamin D ₃ synthesis									
MRE	−3.38	0.89	12.33	1.26	1.98	6.65	−1.97	0.83	6.32
MAE	10.09	12.14	21.75	10.46	11.59	17.05	10.62	11.97	15.32
RMSE	15.92	18.14	27.55	14.54	16.10	21.85	15.34	16.50	19.98
SD	15.56	18.13	24.64	14.49	15.98	20.82	15.22	16.49	18.96
psoriasis clearance									
MRE	−3.91	−1.55	2.91	−0.16	−0.41	0.17	−1.95	−0.02	1.82
MAE	9.93	11.52	18.48	10.08	10.52	14.28	10.30	11.30	13.30
RMSE	15.68	17.75	24.96	14.52	15.36	20.27	14.83	15.83	18.75
SD	15.19	17.69	24.80	14.52	15.36	20.27	14.71	15.84	18.66
SARS-CoV-2 virions inactivation									
MRE	−3.47	−5.78	−4.40	−0.41	−2.86	−3.65	3.11	2.02	1.93
MAE	8.26	12.02	19.47	7.83	9.01	13.56	8.72	10.00	12.93
RMSE	12.99	18.01	25.92	11.78	13.93	20.37	11.79	13.58	18.28
SD	12.52	17.06	25.56	11.77	13.64	20.04	11.38	13.43	18.18

The UBE model with the cloud effect parameterization based on $\hat{\alpha}_{\text{ERYT}}$ and $\hat{\beta}_{\text{ERYT}}$ performs better (i.e., in terms of the statistical metrics closer to zero) than the UBE model with $\hat{\alpha}_{\text{BIOL}}$ and $\hat{\beta}_{\text{BIOL}}$ (i.e., each effect has its own cloud attenuation coefficients) in ~80% of the metrics (86 cases out of a total 108 cases) and ~92% (33 cases out of a total 36 cases) for any SZA at noon and SZA_N < 45°, respectively. For the range of SZA_N with the highest

UV intensity ($SZA_N < 45^\circ$), MRE and SD values are between -4% and 3% and $\sim 11\text{--}16\%$, respectively, for the UBE model with $\hat{\alpha}_{ERYT}$ and $\hat{\beta}_{ERYT}$. Whereas, for $SZA_N < 60^\circ$, MRE and SD are in the range between -6% and 3% and $11\text{--}18\%$, respectively.

The TEMIS_UV data also includes simulated $RE_{VITD}(D)$ for several ground stations, including Belsk, Uccle, and Reading. It is, therefore, worth evaluating the performance of this product and comparing it to the UBE model by calculating statistical metrics of differences between the TEMIS overpass data for the above stations and the directly derived $RE_{VITD}(D)$ from the spectral radiometers. Table A2 shows the performance of the TEMIS_UV model for the three stations. Comparing these results with the corresponding results shown in Table 8, a better agreement with the measured data can be revealed for the UBE model as 100% of the metrics values were closer to zero when $SZA_N < 60^\circ$. TEMIS_UV performs better than the UBE model for 75% of metric values when $SZA_N > 60^\circ$, which is the case in winter with less attention to solar UV radiation, which is usually weak during this period.

Figure 4 shows that the results of the UBE model with $\hat{\alpha}_{ERYT}$ and $\hat{\beta}_{ERYT}$ are consistent with the corresponding values from the spectral measurements at Belsk for the entire UV variability range when $SZA_N < 45^\circ$. For other stations, similar agreement was found (Figure A3).

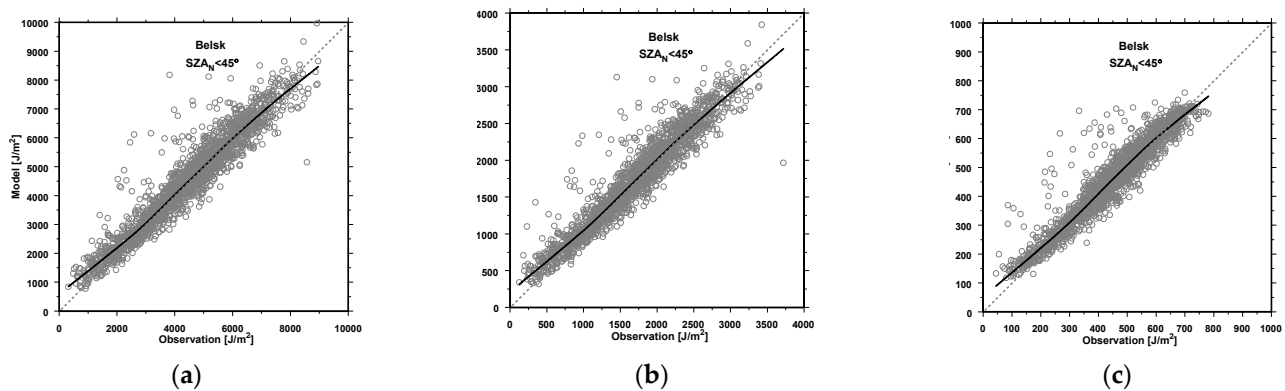


Figure 4. Scatter plot $RE_{BIOL}(D)$ from the UBE model with $\hat{\alpha}_{ERYT}$ and $\hat{\beta}_{ERYT}$ when $SZA_N < 45^\circ$ versus corresponding values from spectral measurements at Belsk for the period 2011–2023: (a) for VITD, (b) for PSOR, and (c) for SARS.

4. Discussion

Various approaches to modeling UV radiation for all sky conditions have been explored, including, for example, the use of the full radiative transfer model option, which requires detailed information on ozone (column amount and vertical profile), aerosols and cloud characteristics [44], the use of a synthetic clear-sky value combined with empirical relationships for the effect of clouds on solar attenuation (proposed model), and the use of artificial intelligence (e.g., neural network techniques [45]). The second and third options for UV modeling, with ground-based observations providing various proxies for UV calculations, were applied to eight sites in Europe with calibrated UV measurements via biometers [45]. Global solar irradiance appeared of special importance for explaining UV variability. The SD for the ratio of modeled-to-measured daily ERE for all-sky conditions varied between 8% and 36% depending on the combination of the UV model and site. The differences between the measured and modeled daily ERE were approximately from -3% up to 13%.

In the present study, for low and medium SZA ($SZA_N < 60^\circ$), despite the use of satellite-derived global solar radiation, the results of the UBE model for five stations (Belsk, Reading, Uccle, Diekirch, and Vienna) were similar to those shown in [45] based on the UV explanatory variables from ground-based measurements. Comparisons of the erythemal data from the observations and UBE model resulted in an MRE and SD in the range $[-8\%, 4\%]$ and $[13\%, 18\%]$, respectively (Tables 3 and 4). Smaller differences were

found for lower SZA at midday ($SZA_N < 45^\circ$), which corresponds to the early spring–late summer season when UV variability is of great public interest. Namely, MRE and SD were in the range $[-5\%, 0\%]$ and $[13\%, 16\%]$, respectively. Larger differences appeared for $SZA_N > 60^\circ$ with an MRE and SD in the range $[-19\%, 4\%]$ and $[18\%, 27\%]$, respectively, as MSG radiation product is less accurate for $SZA > 70^\circ$ [46]. However, $SZA_N > 60^\circ$ in Europe occurs in late autumn and winter (Table A1), when UV intensity is low and biological effects are much less dependent on solar radiation.

The UBE model performs better than the two free-access models (OMI_UV and Temis_UV), providing regular updates of surface UV radiation from space. In observation–model comparisons, the data were analyzed for Belsk, Davos, Diekirch (only for OMI_UV), Reading, Uccle, and Vienna. The station in Chisinau was not included in the analyses due to calibration problems. In the case of comparison with TEMIS_UV, the UBE model provided lower values of statistical metrics (absolute value of MSR, MAE, RMSE, and SD) in ~90% of the metrics (54 cases out of total of 60 cases = 5 number of stations \times 3 ranges of $SZA_N \times$ 4 total number of the metrics). For the comparison with OMI_UV, lower metrics values were found in ~93% of the metrics (67 cases out of total of 72 cases = 6 number of stations \times 3 number of SZA_N ranges \times 4 number of metrics).

The UBE version for the erythemal effects provides a good estimate of the daily ERE at the ground level, especially at snow-free locations when SZA at noon is below 45° , since the MRE and SD of the differences between measurements and the model data are in the ranges of $[-5\%, 0\%]$ and $[13\%, 17\%]$, respectively, considering the UV observations at Belsk, Davos (Table 5 for snow-free days), Diekirch, Reading, Uccle, and Vienna.

OMI_UV and TEMIS_UV include information on the surface albedo (climatological values to model seasonal changes in albedo). This is not explicitly used in UBE, but the snow effects are indirectly included in the model as the SEVIRI algorithm accounts for the amplification of global solar radiation due to the snow reflectivity. This gives a possibility to model erythemal radiation at the surface when snow is present. Table 5 shows that UBE performance in such conditions was even better than TEMIS_UV, but both models provided large underestimation (about 20% and 40%, respectively) of the daily ERE during the snow period. This suggests that satellite UV estimates for mountain stations should be treated with caution during the cold part of the year. Furthermore, the snow occurred at a time when SZA at midday is high, and the MSG radiation product is then less accurate [46].

Currently, there are only broadband instruments (biometers) designed to measure erythemal irradiance. Therefore, non-erythemal irradiance may be available from less frequent ground-based spectral measurements, and data for larger areas can only be obtained from satellites. In this case, UV spectra were available from three stations: Belsk, Reading, and Uccle. The UBE model uses the conversion factor from the erythemal irradiance to the non-erythemal irradiance [20] to calculate the non-erythemal irradiance for cloudless-sky conditions. This does not lead to lower accuracy of the non-erythemal UBE model with respect to its erythemal version. Comparisons of the measurements and non-erythemal UBE model (Table 8) resulted in an MRE and SD in the range $[-4\%, 3\%]$ and $[11\%, 16\%]$, respectively, when $SZA_N < 45^\circ$ (Table 8). For $SZA_N < 60^\circ$, the MRE and SD were in the range $[-6\%, 3\%]$ and $[11\%, 18\%]$, respectively.

All action spectra considered (Figure 1) have a fairly similar pattern with a rapid decrease with wavelength. For such patterns, no significant differences were found in the attenuation of biologically weighted irradiance due to clouds depending on the biological effects considered. The UBE model with $\hat{\alpha}_{ERYT}$ and $\hat{\beta}_{ERYT}$ performed even better than the UBE model with the cloud attenuation coefficients for a specific biological effect. This appears in 89% of the metrics (64 cases out of 72 cases for SZA at midday less than 60°) when comparing MRE, MAE, RMSE, and SD in Tables 7 and 8. Therefore, it can be hypothesized that the erythemal cloud attenuation coefficients, $\hat{\alpha}_{ERYT}$ and $\hat{\beta}_{ERYT}$, could be effectively used to parameterize the cloud effects for any biologically effective radiation with a similar rapidly decreasing action spectrum with wavelength.

Potential users of the model are scientists involved in studying long-term changes in UV radiation associated with climate change. Possible areas of interest could be the identification of sources of UV changes (i.e., estimating the contribution of TCO_3 , clouds, and aerosols to long-term changes in surface UV radiation) and the search for regional changes in UV intensity to delineate ‘hot spots’ with abnormal UV levels. It is expected that knowledge of UV radiation for any location (in the MSG area) will be valuable for those looking for health and environmental impacts of UV radiation. In this way, a kind of balance between harmful and beneficial UV effects on health and the environment can be established in locations where no ground-based UV observations are made.

The proposed model can be used not only to retrieve UV estimates for any location within the MSG area. In addition, it provides a tool for testing the quality of UV measurement data with biometers and a parameterization of clouds’ effect on surface UV. The need for the calibration of individual station data arises when the differences between the observations and the modeled daily ERE in the model/observations scatter plot differ significantly from the ideal 1–1 line of agreement, as was the case for measurements in Chisinau (Figure A2).

5. Conclusions

The proposed model allows for the estimation of the biologically effective daily radiation exposure for any location in the MSG area for any biological effect with a known formula for its action spectrum without validation for each new location. The power function of CI calculated from the SEVIRI global solar irradiance product can effectively parameterize the impact of clouds on biologically effective irradiance at the Earth’s surface. In the case of erythral effects, in addition to the fixed local parameters (latitude, longitude, altitude, and climatological value of horizontal visibility), only CI, SZA, and TCO_3 (here, from the MERRA-2 reanalysis) are the variable parameters needed to run the model. For non-erythral effects, the conversion factor from erythral to other non-erythral radiation irradiance must be used, which also depends on SZA and TCO_3 . This has been tabulated previously for SZA \times TCO_3 pairs using the action spectra previously considered in Czerwińska and Krzyścin [20]. For new action spectra, the conversion factors could be easily calculated from the radiative transfer model for clear-sky conditions. If any new UV-sensitive biological process emerges (e.g., a new variant of COVID-19), it will be possible to estimate the corresponding biologically effective exposure using this model.

The proposed all-sky model is particularly useful in snow-free locations when the SZA at noon is less than 45° . Such conditions reflect the period when the UV intensity is considered most important for human health. The expected bias and standard deviation of the measurement–model differences are about $\pm 5\%$ and 15%, respectively, regardless of the biological effect considered.

Author Contributions: Conceptualization, A.C. and J.K.; methodology, J.K.; software, A.C.; validation, A.C.; formal analysis, J.K.; investigation, A.C. and J.K.; resources, A.C.; data curation, A.C.; writing—original draft preparation, A.C. and J.K.; writing—review and editing, A.C. and J.K.; visualization, A.C.; supervision, J.K.; project administration, A.C.; funding acquisition, A.C. and J.K. All authors have read and agreed to the published version of the manuscript.

Funding: This research received no external funding.

Data Availability Statement: The archived data used are listed in Table 1.

Conflicts of Interest: The authors declare no conflicts of interest.

Appendix A

Table A1. Dates: when the noon SZA (SZA_N) is below 45° , above 45° and below 60° , and above 60° , for the stations listed in Table 1 (calculated for a non-leap year).

Station	$SZA_N < 45^\circ$	$SZA_N \geq 45^\circ$ and $SZA_N < 60^\circ$	$SZA_N \geq 60^\circ$
Belsk (Poland)	8 April–5 September	28 February–7 April 6 September–14 October	1 January–27 February 15 October–31 December
Reading (UK)	6 April–6 September	27 February–5 April 7 September–15 October	1 January–26 February 16 October–31 December
Uccle (Belgium)	4 April–7 September	25 February–3 April 8 September–17 October	1 January–24 February 18 October–31 December
Vienna (Austria)	29 March–14 September	18 February–28 March 15 September–23 October	1 January–17 February 24 October–31 December
Diekirch (Luxembourg)	2 April–10 September	23 February–1 April 11 September–19 October	1 January–22 February 20 October–31 December
Davos (Switzerland)	26 March–18 September	14 February–25 March 19 September–28 October	1 January–13 February 29 October–1 December
Chisinau (Moldavia)	26 March–17 September	15 February–25 March 18 September–27 October	1 January–14 February 28 October–31 December

Table A2. Performance of the TEMIS_UV model for estimation of daily radiant exposures for previtamin D₃ synthesis using TEMIS overpass data and results of the spectral measurements in the 2004–2013 period (for Uccle and Reading) and in the 2011–2013 period (for Belsk).

Statistics [%]	Belsk			Uccle			Reading		
	$SZA_N < 45^\circ$	$SZA_N [45^\circ, 60^\circ]$	$SZA_N > 60^\circ$	$SZA_N < 45^\circ$	$SZA_N [45^\circ, 60^\circ]$	$SZA_N > 60^\circ$	$SZA_N < 45^\circ$	$SZA_N [45^\circ, 60^\circ]$	$SZA_N > 60^\circ$
MRE	−17.15	−6.49	−6.63	−13.67	−6.74	−1.68	−17.18	−9.14	−2.17
MAE	18.17	15.42	18.06	15.03	11.91	15.71	18.52	13.02	14.38
RMSE	24.84	22.83	24.96	21.68	18.08	21.68	25.04	18.97	20.08
SD	17.98	21.94	24.10	16.83	16.79	21.62	18.23	16.63	19.97

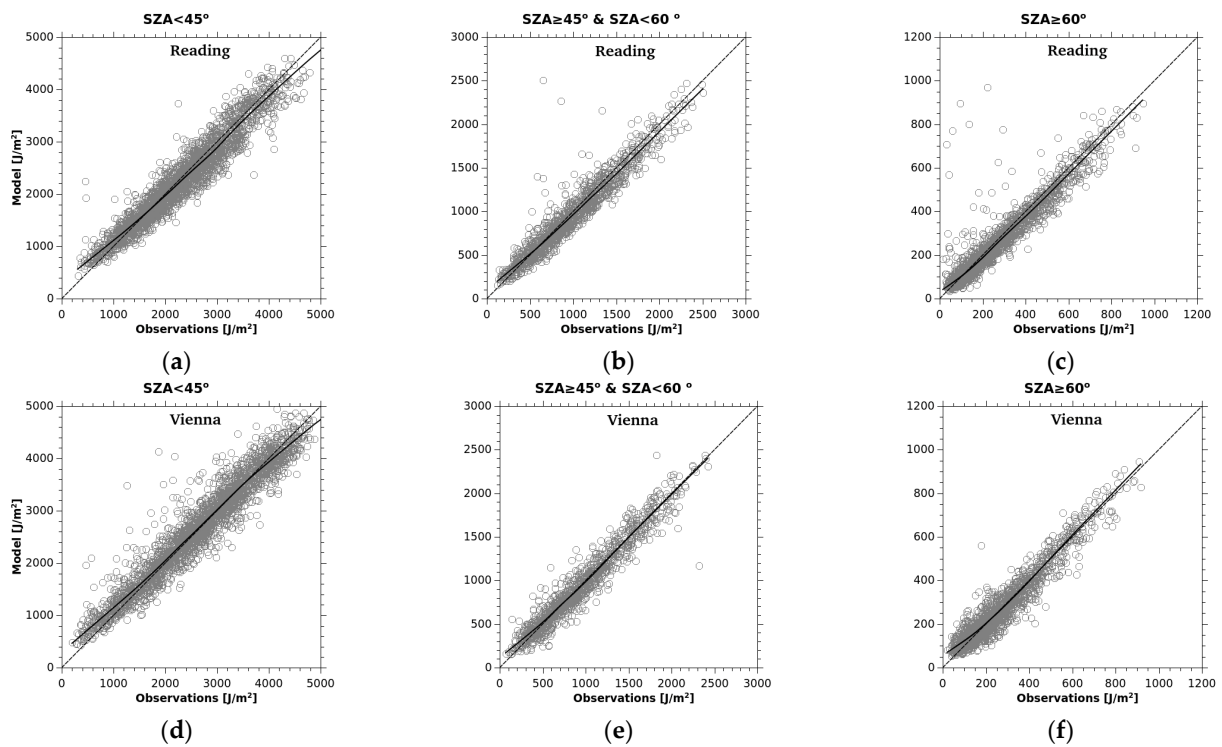


Figure A1. Scatter plot of the modeled (UBE model with $\hat{\alpha}_{ERYT}$ and $\hat{\beta}_{ERYT}$) versus the measured daily radiant exposure for all-sky conditions and different ranges of SZA at noon: (a) Reading for $SZA_N < 45^\circ$; (b) Reading for $SZA_N \geq 45^\circ$ and $SZA_N < 60^\circ$; (c) Reading for $SZA \geq 60^\circ$; (d) Vienna for $SZA_N < 45^\circ$; (e) Vienna for $SZA_N \geq 45^\circ$ and $SZA_N < 60^\circ$; (f) Vienna for $SZA \geq 60^\circ$. The dotted line is the 1–1 agreement line. The solid curve represents smoothed values from the Lowess filter [43].

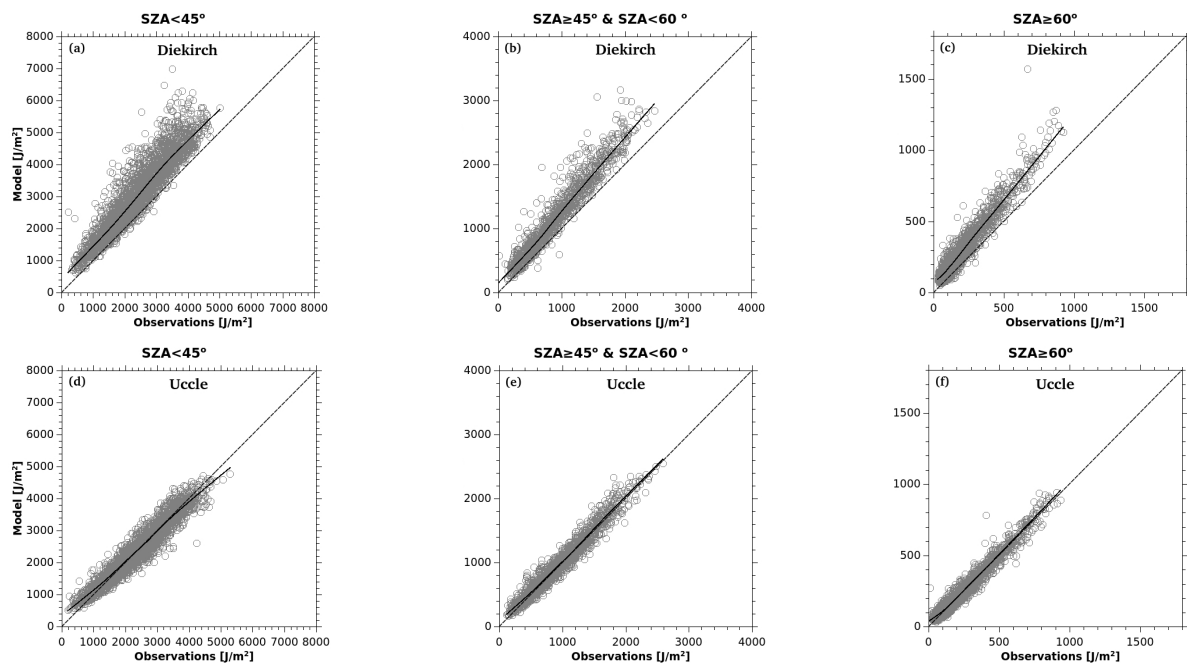


Figure A2. Cont.

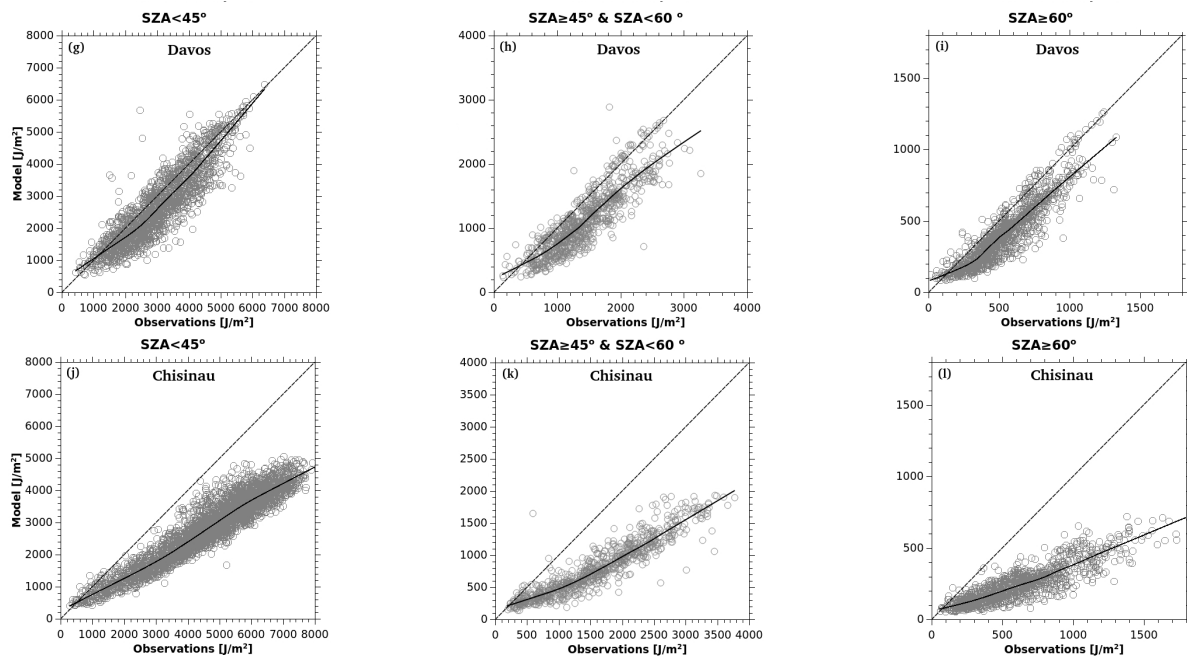


Figure A2. Scatter plot of the modeled (UBE model with $\hat{\alpha}_{ERYT}$ and $\hat{\beta}_{ERYT}$) versus measured daily erythemal radiant exposure for different ranges of noon SZA: ($SZA < 45^\circ$; $SZA \geq 45^\circ$ and $SZA < 60^\circ$; and $SZA \geq 60^\circ$): (a–c) Diekirch (Luxembourg); (d–f) Uccle (Belgium); (g–i) Davos (Switzerland); (j–l) Chisinau (Moldavia). As these stations were not used in UBE training, all available daily data in the period 2004–2023 have been used. The dotted line is the 1–1 perfect agreement line. The solid curve represents smoothed values from the Lowess filter [43].

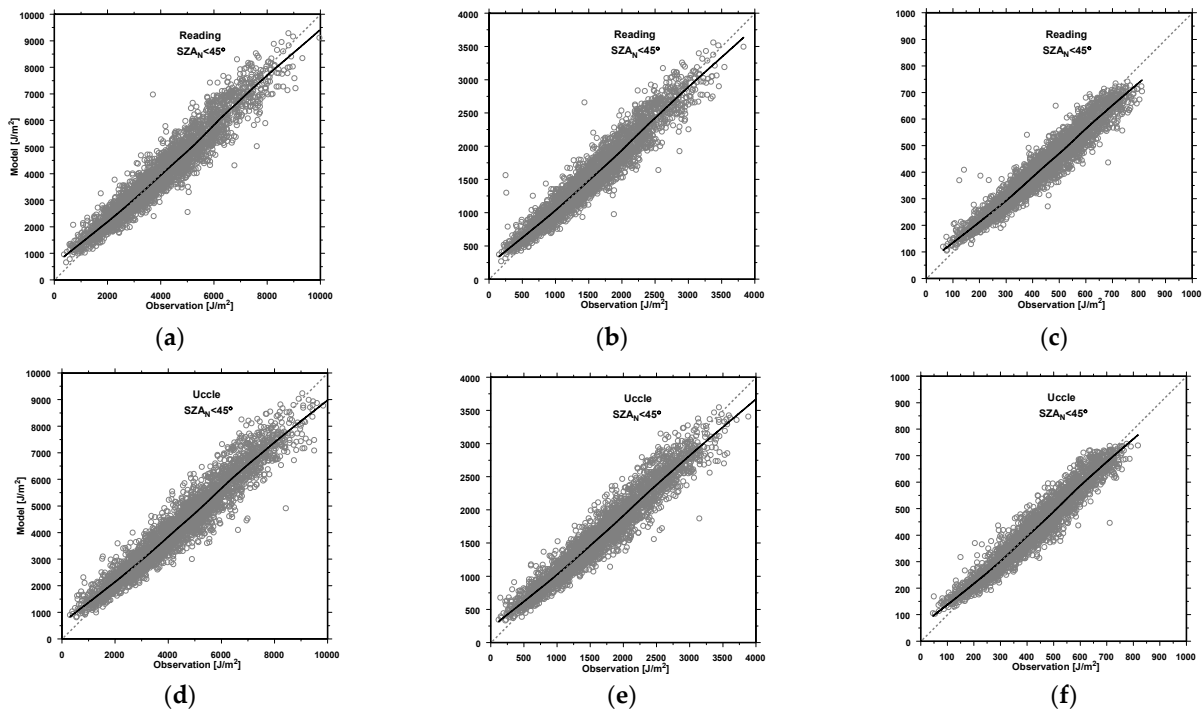


Figure A3. Scatter plot of the modeled (UBE model with $\hat{\alpha}_{ERYT}$ and $\hat{\beta}_{ERYT}$) versus the measured daily radiant exposure for all-sky conditions and SZA at noon less than 45° : (a) VITD for Reading; (b) PSOR for Reading; (c) SARS for Reading; (d) VITD for Uccle; (e) PSOR for Uccle; (f) SARS for Uccle. The dotted line is the 1–1 agreement line. The solid curve represents smoothed values from the Lowess filter [43].

References

- Berger, D.S.; Urbach, F. A climatology of sunburning ultraviolet radiation. *Photochem. Photobiol.* **1982**, *35*, 187–192. [[CrossRef](#)] [[PubMed](#)]
- Holick, M.F.; Chen, T.C. Vitamin D deficiency: A worldwide problem with health consequences. *Am. J. Clin. Nutr.* **2008**, *87*, 1080S–1086S. [[CrossRef](#)] [[PubMed](#)]
- Sivamani, R.K.; Crane, L.A.; Dellavalle, R.P. The benefits and risks of ultraviolet tanning and its alternatives: The role of prudent sun exposure. *Dermatol. Clin.* **2009**, *27*, 149–154. [[CrossRef](#)] [[PubMed](#)]
- Krzyściński, J.W.; Guzikowski, J.; Rajewska-Więch, B. Optimal vitamin D3 daily intake of 2000IU inferred from modeled solar exposure of ancestral humans in Northern Tanzania. *J. Photochem. Photobiol. B Biol.* **2016**, *159*, 101–105. [[CrossRef](#)] [[PubMed](#)]
- Young, A.R. Acute effects of UVR on human eyes and skin. *Prog. Biophys. Mol. Biol.* **2006**, *92*, 80–85. [[CrossRef](#)]
- Krzyściński, J.W.; Narbutt, J.; Lesiak, A.; Jarosławski, J.; Sobolewski, P.S.; Rajewska-Więch, B.; Szkop, A.; Wink, J.; Czerwińska, A. Perspectives of the antipsoriatic heliotherapy in Poland. *J. Photochem. Photobiol. B Biol.* **2014**, *140*, 111–119. [[CrossRef](#)]
- Liu, D.; Fernandez, B.O.; Hamilton, A.; Lang, N.N.; Gallagher, J.M.; Newby, D.E.; Feelisch, M.; Weller, R.B. UVA irradiation of human skin vasodilates arterial vasculature and lowers blood pressure independently of nitric oxide synthase. *J. Invest. Dermatol.* **2014**, *134*, 1839–1846. [[CrossRef](#)]
- Bernhard, G.H.; Madronich, S.; Lucas, R.M.; Byrne, S.N.; Schikowski, T.; Neale, R.E. Linkages between COVID-19, solar UV radiation, and the Montreal protocol. *Photochem. Photobiol. Sci.* **2023**, *22*, 991–1009. [[CrossRef](#)]
- Biasin, M.; Strizzi, S.; Bianco, A.; Macchi, A.; Utyro, O.; Pareschi, G.; Loffreda, A.; Cavalleri, A.; Lualdi, M.; Trabattoni, D.; et al. UV and violet light can neutralize SARS-CoV-2 infectivity. *J. Photochem. Photobiol.* **2022**, *10*, 100107. [[CrossRef](#)]
- Lucas, R.M.; Yazar, S.; Young, A.R.; Norval, M.; de Grijl, F.R.; Takizawa, Y.; Rhodes, L.E.; Sinclair, C.A.; Neale, R.E. Human health in relation to exposure to solar ultraviolet radiation under changing stratospheric ozone and climate. *Photochem. Photobiol. Sci.* **2019**, *18*, 641–680. [[CrossRef](#)]
- Berger, D.S. The sunburning ultraviolet meter: Design and performance. *Photochem. Photobiol.* **1976**, *24*, 587–593. [[CrossRef](#)] [[PubMed](#)]
- Słomka, J.; Słomka, K. Biologically active solar UV radiation at Belsk in years 1976–1992. *Inst. Geophys. Pol. Acad. Sci.* **1993**, *D-40*, 71–81.
- Josefsson, W. UV-radiation 1983–2003 measured at Norrköping, Sweden. *Theor. Appl. Climatol.* **2006**, *83*, 59–76. [[CrossRef](#)]
- Hülsen, G.; Gröbner, J. Characterization and calibration of ultraviolet broadband radiometers measuring erythemally weighted irradiance. *Appl. Opt.* **2007**, *46*, 5877–5886. [[CrossRef](#)] [[PubMed](#)]
- Schmalwieser, A.W.; Gröbner, J.; Blumthaler, M.; Klotz, B.; De Backer, H.; Bolsée, D.; Werner, R.; Tomsic, D.; Metelka, L.; Eriksen, P.; et al. UV index monitoring in Europe. *Photochem. Photobiol. Sci.* **2017**, *16*, 1349–1370. [[CrossRef](#)]
- Tanskanen, A.; Lindfors, A.; Määttä, A.; Krotkov, N.; Herman, J.; Kaurola, J.; Koskela, T.; Lakkala, K.; Fioletov, V.; Bernhard, G.; et al. Validation of daily erythemal doses from Ozone Monitoring Instrument with ground-based UV measurement data. *J. Geophys. Res.* **2007**, *112*, D24S44. [[CrossRef](#)]
- Zempila, M.-M.; van Geffen, J.H.; Taylor, M.; Fountoulakis, I.; Koukouli, M.-E.; van Weele, M.; van der A, R.J.; Bais, A.; Meleti, C.; Balis, D. TEMIS UV product validation using NILU-UV ground-based measurements in Thessaloniki. *Atmos. Chem. Phys.* **2017**, *17*, 7157–7174. [[CrossRef](#)]
- Dave, J.V. Meaning of successive iteration of the auxiliary equation in the theory of radiative transfer. *Astrophys. J.* **1964**, *140*, 1292–1303. [[CrossRef](#)]
- Allaart, M.; van Weele, M.; Fortuin, P.; Kelder, H. An empirical model to predict the UV-index based on solar zenith angles and total ozone. *Meteorol. Appl.* **2004**, *11*, 59–65. [[CrossRef](#)]
- Czerwińska, A.; Krzyściński, J. Measurements of biologically effective solar radiation using erythemal weighted broadband meters. *Photochem. Photobiol. Sci.* **2024**, *23*, 479–492. [[CrossRef](#)]
- Madronich, S. The atmosphere and UV-B radiation at ground level. In *Environmental UV Photobiology*; Björn, L.O., Young, A.R., Eds.; Springer: Boston, MA, USA, 1993; pp. 1–39.
- Slaper, H.; Reinen, H.; Blumthaler, M.; Huber, M.; Kuik, F. Comparing ground level spectrally resolved UV measurements from various instruments: A technique resolving effects of wavelength shifts and slit width. *Geophys. Res. Lett.* **1995**, *22*, 2721–2724. [[CrossRef](#)]
- ISO/CIE 17166:2019(E); Erythema Reference Action Spectrum and Standard Erythema Dose. CIE: Vienna, Austria, 2019; pp. 1–5.
- Collow, A.; Bosilovich, M.; Dezfuli, A.; Lucchesi, R. *File Specification for MERRA-2 Climate Statistics Products*; GMAO Office Note No. 19 (Version 1.0); 2020; 15p. Available online: <https://gmao.gsfc.nasa.gov/pubs/docs/Collow1253.pdf> (accessed on 9 October 2024).
- Wargan, K.; Labow, G.; Frith, S.; Pawson, S.; Livesey, N.; Partyka, G. Evaluation of the Ozone Fields in NASA's MERRA-2 Reanalysis. *J. Clim.* **2017**, *30*, 2961–2988. [[CrossRef](#)] [[PubMed](#)]
- Coldewey-Egbers, M.; Loyola, D.G.; Labow, G.; Frith, S.M. Comparison of GTO-ECV and adjusted MERRA-2 total ozone columns from the last 2 decades and assessment of interannual variability. *Atmos. Meas. Tech.* **2020**, *13*, 1633–1654. [[CrossRef](#)]
- Gupta, P.; Payra, S.; Bhatla, R.; Verma, S. An evaluation of long-term gridded datasets of total columnar ozone retrieved from MERRA-2 and AIRS over the Indian region. *Environ. Sci. Pollut. Res.* **2023**, *30*, 43586–43603. [[CrossRef](#)] [[PubMed](#)]

28. Liu, B.Y.H.; Jordan, R.C. The Interrelationship and Characteristic Distribution of Direct, Diffuse, and Total Solar Radiation. *Sol. Energy* **1960**, *4*, 1–19. [[CrossRef](#)]
29. CAMS Solar Radiation Time-Series. Available online: <https://ads.atmosphere.copernicus.eu/datasets/cams-solar-radiation-timeseries?tab=overview> (accessed on 26 August 2024).
30. Giovanni: The Bridge between Data and Science v. 4.40. Available online: <https://giovanni.gsfc.nasa.gov/giovanni/> (accessed on 26 August 2024).
31. OMI/Aura Surface UVB Irradiance and Erythral Dose Daily L3 Global Gridded 1.0 Degree x 1.0 Degree V3. NASA Goddard Space Flight Center, Goddard Earth Sciences Data and Information Services Center (GES DISC). Available online: <https://catalog.data.gov/dataset/omi-aura-surface-uvb-irradiance-and-erythral-dose-daily-l3-global-gridded-1-0-degree-x-1-0-degree> (accessed on 26 August 2024).
32. Yesterday's UV Dose and Archives. Available online: <https://www.temis.nl/uvradiation/UVdose.php> (accessed on 26 August 2024).
33. UV Station Data Based on Operational TEMIS Satellite Ozone Data. Available online: https://www.temis.nl/uvradiation/UVarchive/stations_uv.php (accessed on 28 August 2024).
34. CIE 174:2006; Action Spectrum for the Production of Previtamin D3 in Human Skin. CIE: Vienna, Austria, 2006; pp. 1–16.
35. Krzyścin, J.W.; Jarosławski, J.; Rajewska-Więch, B.; Sobolewski, P.S.; Narbutt, J.; Lesiak, A.; Pawlaczyk, M. Effectiveness of heliotherapy for psoriasis clearance in low and mid-latitudinal regions: A theoretical approach. *J. Photochem. Photobiol. B Biol.* **2012**, *115*, 35–41. [[CrossRef](#)]
36. Vanicek, K.; Frei, T.; Litynska, Z.; Schmalwieser, A. *UV-Index for the Public*; COST-713 Action; Publication of the European Communities: Brussels, Belgium, 2000; pp. 1–27.
37. Engelsen, O.; Kylling, A. Fast simulation tool for ultraviolet radiation at the earth's surface. *Opt. Eng.* **2005**, *44*, 041012. [[CrossRef](#)]
38. Majewski, G.; Rogula-Kozłowska, W.; Czechowski, P.O.; Badyda, A.; Brandyk, A. The impact of selected parameters on visibility: First results from a long-term campaign in Warsaw, Poland. *Atmosphere* **2015**, *6*, 1154–1174. [[CrossRef](#)]
39. Singh, A.; Bloss, W.J.; Pope, F.D. 60 years of UK visibility measurements: Impact of meteorology and atmospheric pollutants on visibility. *Atmos. Chem. Phys.* **2017**, *17*, 2085–2101. [[CrossRef](#)]
40. Horvath, H. On the applicability of the Koschmieder visibility formula. *Atmos. Environ.* **1971**, *5*, 177–184. [[CrossRef](#)]
41. Aeronet Aerosol Optical Depth. Available online: https://aeronet.gsfc.nasa.gov/new_web/climo_menu_new_v3.html (accessed on 26 August 2024).
42. Schmalwieser, A.W.; Eschenbacher, S.; Schreder, J. UV-Biometer—The usage of erythral weighted broadband meters for other biological effects. *J. Photochem. Photobiol. B Biol.* **2022**, *230*, 112442. [[CrossRef](#)] [[PubMed](#)]
43. Cleveland, W.S. Robust Locally Weighted Regression and Smoothing Scatterplots. *J. Am. Stat. Assoc.* **1979**, *74*, 829–836. [[CrossRef](#)]
44. Kosmopoulos, P.G.; Kazadzis, S.; Schmalwieser, A.W.; Raptis, P.I.; Papachristopoulou, K.; Fountoulakis, I.; Masoom, A.; Bais, A.F.; Bilbao, J.; Blumthaler, M.; et al. Real-time UV index retrieval in Europe using Earth observation-based techniques: System description and quality assessment. *Atmos. Meas. Tech.* **2021**, *14*, 5657–5699. [[CrossRef](#)]
45. den Outer, P.N.; Slaper, H.; Kaurola, J.; Lindfors, A.; Kazantzidis, A.; Bais, A.F.; Feister, U.; Junk, J.; Janouch, M.; Josefsson, W. Reconstructing of erythral ultraviolet radiation levels in Europe for the past 4 decades. *J. Geophys. Res.* **2010**, *115*, D10102. [[CrossRef](#)]
46. Kato, S.; Marshak, A. Solar zenith and viewing geometry-dependent errors in satellite retrieved cloud optical thickness: Marine stratocumulus case. *J. Geophys. Res.* **2009**, *114*, D01202. [[CrossRef](#)]

Disclaimer/Publisher's Note: The statements, opinions and data contained in all publications are solely those of the individual author(s) and contributor(s) and not of MDPI and/or the editor(s). MDPI and/or the editor(s) disclaim responsibility for any injury to people or property resulting from any ideas, methods, instructions or products referred to in the content.